Postseismic motion after the 2001 M_W 7.8 Kokoxili earthquake in Tibet observed by InSAR time series

Yangmao Wen,[1,2,3] Zhenhong Li,[3] Caijun Xu,[1,2] Isabelle Ryder,[4] and Roland Bürgmann[5]

Received 21 November 2011; revised 6 June 2012; accepted 20 June 2012; published 9 August 2012.

[1] On November 14th 2001, a Mw 7.8 earthquake occurred in the Kokoxili region of northern Tibet. The earthquake ruptured more than 400 km along the western part of the Kunlun fault with a maximum of 8 m left-lateral slip. In this paper, we use a multitemporal Interferometric SAR (InSAR) time series technique to map the postseismic motion following the large Kokoxili event. SAR data from Envisat descending orbits along five adjacent tracks covering almost the entire ruptured fault length are used to calculate the displacement time series for a period between 2 and 6 years after the earthquake. A peak-to-trough signal of 8 cm in the radar line of sight is observed during the period between 2003 and 2008. Two different mechanisms are employed to explain the observed surface displacements, namely afterslip and viscoelastic relaxation. The observations inverted for afterslip on and below the coseismic rupture plane shows that the maximum slip in the afterslip model is 0.6 m. The position of the maximum postseismic slip is located in the middle of two relatively high coseismic slip patches, which suggests that afterslip is a plausible mechanism. Models of viscoelastic stress relaxation in a Maxwell half-space give a best fitting viscosity for the mid-to-lower crust of 2–5 $\times$ 10^{19} Pa s, and the principal postseismic relaxation process is due to viscous flow in the lower crust to upper mantle. However, the InSAR observations are incapable of distinguishing between localized (afterslip) and distributed (viscoelastic relaxation) deformation. And the lowest misfits are produced by mixed models of viscoelastic relaxation in the mantle below 70 km and afterslip in the crust. Modeling of viscoelastic relaxation in a Maxwell half-space, and also a mixed mechanism model, enables us to place an effective viscosity of 2 $\times$ 10^{19} Pa s on the lower crust to mantle of northern Tibet.

Citation: Wen, Y., Z. Li, C. Xu, I. Ryder, and R. Bürgmann (2012), Postseismic motion after the 2001 M_W 7.8 Kokoxili earthquake in Tibet observed by InSAR time series, *J. Geophys. Res.*, *117*, B08405, doi:10.1029/2011JB009043.

1. Introduction

[2] Postseismic motion following large earthquakes represents the response of host rocks to the redistribution of coseismic stress changes. Geodetic and seismic observations show that postseismic displacements are typically an order of magnitude smaller than coseismic displacements and decrease with time over a period of years following the event. Geodetic measurements of postseismic motion are generally proposed to be a result of (1) afterslip on unruptured fault patches near the surface or downdip of the coseismic rupture [e.g., *Marone et al.*, 1991; *Bürgmann et al.*, 2002]; (2) viscoelastic deformation of the lower crust and/or upper mantle [e.g., *Pollitz et al.*, 2000], where coseismic stress changes imparted to the hot lower crust and upper mantle cannot be sustained and drive viscoelastic flow; and/or (3) poroelastic rebound [e.g., *Peltzer et al.*, 1998; *Jónsson et al.*, 2003], where coseismic pressure changes drive fluid flow within the upper crust. Each mechanism is capable of producing observable surface displacements and can operate separately or in combination [e.g., *Fialko*, 2004; *Freed et al.*, 2006a; *Biggs et al.*, 2009]. Although different mechanisms can produce spatially similar displacement fields [*Savage*, 1990; *Hearn*, 2003], surface displacements with a good spatial and temporal resolution over time periods ranging from days to years following the earthquake are more helpful in identifying what is happening at depth, which might provide insight into future seismic hazards.

[3] On November 14th 2001, a Mw 7.8 earthquake struck the Kokoxili region of northern Tibet; no casualties were reported, due to the extremely low population density and

[1]School of Geodesy and Geomatics, Wuhan University, Wuhan, China.
[2]Key Laboratory of Geospace Environment and Geodesy, Ministry of Education, China, Wuhan, China.
[3]COMET+, School of Geographical and Earth Sciences, University of Glasgow, Glasgow, UK.
[4]School of Environmental Sciences, University of Liverpool, Liverpool, UK.
[5]Berkeley Seismological Laboratory, University of California, Berkeley, California, USA.

Corresponding author: C. Xu, School of Geodesy and Geomatics, Wuhan University, Luoyu Rd. 129, Wuhan, Hubei 430079, China. (cjxu@sgg.whu.edu.cn)

0148-0227/12/2011JB009043

the lack of high buildings in the remote region. Surface ruptures of the 2001 Kokoxili earthquake extended over 426 km in total, with an azimuth averaging N100° ± 10°E [*van der Woerd et al.*, 2002b; *Lasserre et al.*, 2005; *Xu et al.*, 2006; *Klinger et al.*, 2006]. The rupture initiated west of Taiyang Lake, on a secondary strike-slip fault within the complex horsetail system that forms the western end of the Kunlun fault. It then propagated eastward, breaking through a 45 km long and 10 km wide pull-apart, to merge with the main trace of the Kunlun fault. The rupture continued on the Kunlun Pass fault along the southern front of the Burchan Budai Shan, ending just east of 95°E [*van der Woerd et al.*, 2002b; *Antolik et al.*, 2004]. The observed displacements essentially correspond to pure left-lateral strike-slip motion on subvertical faults. In a field study, *Xu et al.* [2006] reported a maximum coseismic horizontal left-lateral displacement of 7.6 m (at 35.767°N, 93.323°E). Analysis from 1 m resolution IKONOS and 0.61 m resolution Quickbird images suggests that the coseismic strike-slip offsets range from 2 m up to 16.7 m, but are generally between 3 and 8 m [*Lin and Nishikawa*, 2007]. Using 4 adjacent tracks of ERS InSAR images, *Lasserre et al.* [2005] estimated a maximum left-lateral slip of ∼8 m occurring at depths between 0 and 5 km using a strike-slip model with distributed slip. Both the rupture length and maximum coseismic displacement are the largest ever reported for an intraplate earthquake [*Yeats et al.*, 1997].

[4] *Shen et al.* [2003] modeled 6 months of postseismic Global Positioning System (GPS) data for the Kokoxili earthquake and suggested that both afterslip and viscoelastic relaxation occurred in a lower crustal weak layer. Using one year of GPS data collected at the same stations as *Shen et al.* [2003], *Ren and Wang* [2005] reported that nearly 50 percent of the total surface deformation took place during the first two weeks, implying that the deformation rate rapidly decreased with time. Combining GPS observations presented in *Ren and Wang* [2005] with 5 descending tracks and one ascending track of Envisat ASAR images collected from early 2003 to early 2007, *Ryder et al.* [2011] inferred that the most likely mechanism of post-seismic stress relaxation is time-dependent distributed creep of viscoelastic material in the lower crust. *Ryder et al.* [2011] selected a single track for time series analysis. They attribute a lower deformation gradient in the GPS displacements north of the Kunlun fault to higher viscosities under the Quaidam Basin. In this paper, an advanced InSAR time series technique is employed to analyze 2003–2008 data collected along all five descending tracks of Envisat ASAR images to construct a wide postseismic deformation map for the 2011 Kokoxili earthquake. We then model the surface deformation as afterslip and/or viscoelastic relaxation. The aim of this exercise is to understand which mechanism is responsible for the observed postseismic deformation, and determine the rheological structure of the upper lithosphere.

2. Geological Background

[5] In northern Tibet, the Kunlun and Altyn Tagh faults are two major strike-slip faults which accommodate the eastward extrusion of Tibet in response to the Indo-Asian collision [*Gan et al.*, 2007; *Tapponnier and Molnar*, 1977; *van der Woerd et al.*, 2002b] (Figure 1). The Kunlun fault, located in the Kunlun mountain range in northern Tibet, extends for nearly ∼1500 km along strike, delineating a transition from a low-relief, high-elevation plateau in the south to a northern domain characterized by active high mountain ranges and intramontane basins [*Kirby et al.*, 2007]. The Kunlun fault is also coincident with the northern boundary of the Songpan-Ganzi-Hoh Xil Terrane along the Kunlun suture [*Yin and Harrison*, 2000]. Studies of satellite images, cosmogenic surface dating, radiocarbon dating and trench surveys along the Kunlun fault zone suggest an average slip rate of 10–20 mm/yr during the Quaternary [*van der Woerd et al.*, 2002a; *Lin et al.*, 2006]. Using ^{14}C dating of offset fluvial fans over late Pleistocene to Holocene time, *Kirby et al.* [2007] reported that the slip rates decrease systematically along the eastern ∼150 km of the fault from >10 mm/yr to <2 mm/yr. GPS observations since the 1990s indicate a left-lateral strike slip rate of 10–20 mm/yr on the Kunlun fault [*Wang et al.*, 2001; *Zhang et al.*, 2004; *Hilley et al.*, 2009]. Thus, both geological and GPS data suggest that the slip rate along the Kunlun fault is at the level of ∼10 mm/yr, which indicates that the Kunlun fault plays a key role in models for extrusion of central Tibet [*Li et al.*, 2005].

[6] In the past 100 years, a series of large earthquakes (M ≥ 7) have occurred along the Kunlun fault zone, including the most recent November 14th, 2001 Kokoxili event on the Kusai Hu segment (Figure 1) [*Division of Earthquake Monitoring and Prediction*, 1995, 1999; *Lasserre et al.*, 2005; *Wen et al.*, 2007]. The 1963 Ms 7.0 Alan Lake event and 1937 M 7.5 Dongxi Co event ruptured along the central segment of the Kunlun fault [*Fitch*, 1970; *Jia et al.*, 1988]. The 1973 Ms 7.3 Yiji Taicuo event occurred along the western part of the Manyi fault with an unknown length of surface rupture [*Velasco et al.*, 2000]. In 1997, the Mw 7.6 Manyi earthquake ruptured the westernmost 180 km of the Manyi fault with a maximum left-lateral displacement of 7 m [*Peltzer et al.*, 1999; *Funning et al.*, 2007], which is located to the southwest of the western end of the Kunlun fault and considered as a branch fault of the Kunlun system. Trenching survey studies and offset geomorphological features indicate that the average recurrence interval of great earthquakes on the Kunlun fault falls within the range of ∼300–400 yrs [*van der Woerd et al.*, 2002a; *Li et al.*, 2005; *Lin et al.*, 2006].

[7] Before 31 December 2008, there were ∼115 aftershocks (M ≥ 4) (International Seismological Centre, on-line bulletin, Thatcham, U. K., 2001, http://www.isc.ac.uk) along the Kunlun fault zone (Figure 1). Among these events, the largest aftershock (M 5.6, 4.5 days after the main shock) occurred near the zone of maximum surface offset but was mostly a thrust event. The Kokoxili earthquake has only relatively small aftershocks, all of which were more than two orders of magnitude smaller than the main shock, which is similar to the situation following the Manyi event [*Velasco et al.*, 2000] and the 2002 Denali earthquake [*Bufe*, 2004].

3. InSAR Analysis

[8] InSAR techniques allow us to generate spatially dense maps of ground deformation with tens of meters horizontal spatial resolution over large regions (e.g., 100 km × 100 km). This method uses differences in phase between complex (amplitude and phase) Synthetic Aperture Radar (SAR)

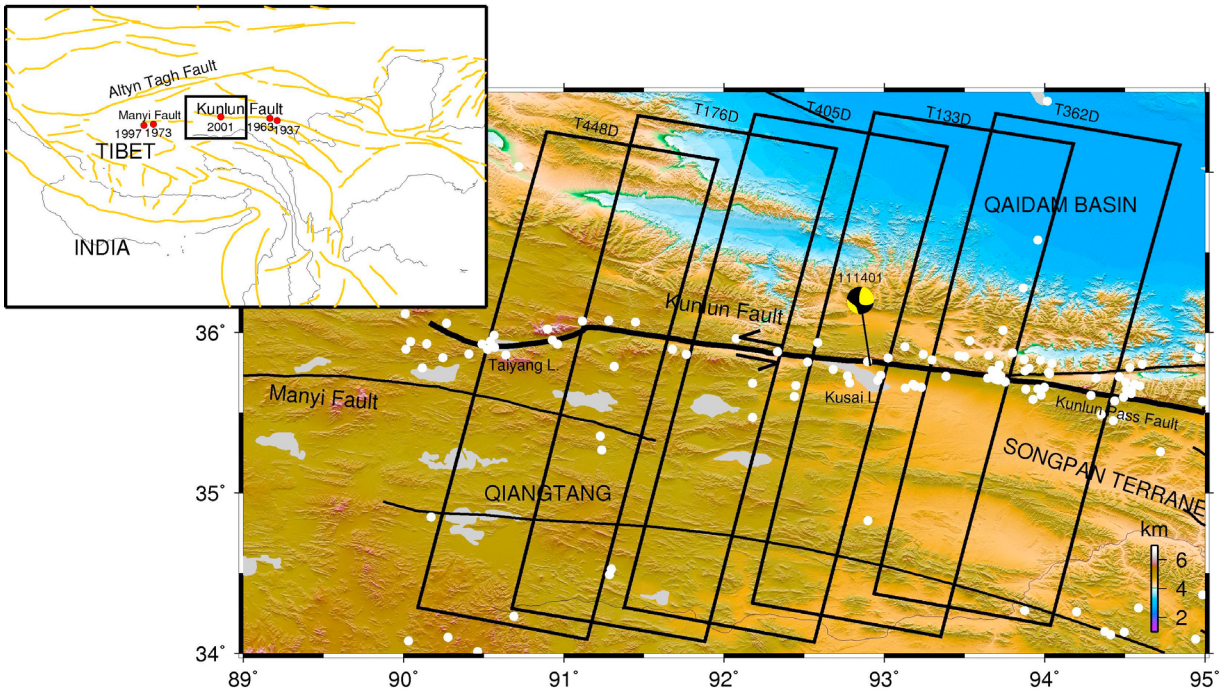

Figure 1. Location map of the western Kunlun fault system superimposed on a 3-arcsecond SRTM DEM. The focal mechanism of the main shock is from the Harvard CMT catalog. White circles represent aftershocks with M ≥ 4.0 (14 November 2001 to 31 December 2008) from International Seismological Centre (on-line bulletin, Thatcham, U. K., 2001, http://www.isc.ac.uk) T448D, T176D, T405D, T133D and T362D refer to 5 adjacent Envisat SAR descending tracks, each marked by black rectangles. Inset map shows location of the Kunlun fault within the India-Asia collision zone. The red circles indicate historical great earthquakes (M ≥ 7) over the past 100 yrs.

images acquired under similar geometric conditions, but at two different epochs to measure the range change between satellite and the Earth surface in the radar line of sight (LOS). With its global coverage and all-weather imaging capability, InSAR has been revolutionizing our ability to image the Earth's surface, which in turn has led to many new insights into geophysical and engineering processes, such as earthquakes, volcanoes, landslides and mining activities [*Massonnet and Feigl*, 1998; *Bürgmann et al.*, 2000; *Rosen et al.*, 2000].

3.1. InSAR Data Sets

[9] The Kokoxili earthquake occurred in November 2001 and Envisat was launched on 1 March 2002. However, no ASAR image was acquired over the study area until April 2003 when the Artemis data relay satellite became available. In this paper, five adjacent descending tracks of ENVISAT images were employed to study the postseismic motion after this large event (Figure 1, track numbers: 448, 176, 405, 133 and 362, and Table 1). Figure S1 in the auxiliary material shows the perpendicular baselines (orbital separations) of all five tracks of ENVISAT images collected over the rupture region, during the period between 2003 and 2008.[1] In this study, all interferograms with a small perpendicular baseline (≤400 m) were produced from the ASAR level 0 (raw data) images using the JPL/Caltech ROI_PAC software (version 3.0) [*Rosen et al.*, 2004], and multilooked to 4 looks in range and 20 in azimuth. Effects of topography were removed from the interferograms using a 3-arc-second posting (~90 m) digital elevation model [*Farr et al.*, 2007] together with the ESA DORIS precision orbits. The interferograms were then filtered using a power spectrum filter [*Goldstein and Werner*, 1998]. The InSAR data set shows better coherence in the north than the south, which may be related to the steep slopes in the Kunlun Mountains region. Moreover, the coherence is better to the south nearer the fault. At such high elevation (>4500 m), temporal decorrelation is probably caused by seasonal snow cover on the summits as well as freeze thaw cycles producing changes in the scattering properties of the surface [*Rosen et al.*, 2000].

[10] Because interferometric phase measurements are modulo 2π radians, integer phase cycle ambiguities must be determined to derive deformation fields, a process known as

Table 1. Details of Data Used in InSAR Time Series Analysis

Track	Date of First Acquisition (yyyy/mm/dd)	Number of Dates	Total Duration (years)
T448D	20031226	12	48.1
T176D	20030720	18	95.5
T405D	20030805	16	90.4
T133D	20030403	19	84.7
T362D	20030628	13	51.0

[1]Auxiliary materials are available in the HTML. doi:10.1029/2011JB009043.

phase unwrapping. In this study, the SNAPHU program [*Chen and Zebker*, 2002] was used to unwrap the phase in 2 dimensions with a coherence threshold of 0.12, and then a phase closure technique [*Biggs et al.*, 2007] was used to identify the major unwrapping errors remaining in the interferograms. The basic idea of the phase closure technique is that phase contributions behave in a conservative manner, i.e., $\phi_{ln} - \phi_{lm} - \phi_{mn} = 0$, where ϕ_{mn} is the phase contribution of interferogram *mn* constructed from acquisitions *n* and *m*. In contrast, phase unwrapping errors do not follow this rule so can be easily identified by summing around a loop and checking the residuals. It is well known that the percentage of coherent areas varies from one interferogram to another due to a range of factors including changes in spatial and/or temporal baselines, and changes in surface properties. Coherent interferograms can be used to verify the unwrapping of other interfergrams with low coherence through the phase closure technique as described in Figure S2. Note that the final area kept in the time series (Section 3.2) used only the pixels that were above the coherence threshold in all independent interferograms. All the major unwrapping errors were identified and manually corrected in this study.

3.2. InSAR Time Series Analysis

[11] In this study, the InSAR Time Series with Atmospheric Estimation Model (InSAR TS + AEM) developed at the University of Glasgow was employed to analyze the unwrapped interferograms, which is based on the SBAS algorithm [*Berardino et al.*, 2002; *Mora et al.*, 2003; *Lundgren et al.*, 2009]. We start with the standard SBAS formulation [*Berardino et al.*, 2002]. Let t be a vector of SAR acquisition dates in chronological order. For a data set containing N interferograms constructed from S acquisitions on different dates, after removing the flat earth and local topography, the unwrapped differential interferometric phase at pixel (x, r) computed from the SAR acquisitions at the start time t_M (for the Master image) and end time t_S (for the Slave image), can be written as follows:

$$\begin{cases} \delta\phi_{t_M t_S}(x,r) = \delta\phi^{topo}_{t_M t_S}(x,r) + \delta\phi^{disp}_{t_M t_S}(x,r) + \delta\phi^{atm}_{t_M t_S}(x,r) + \delta\phi^{noise}_{t_M t_S}(x,r) \\ \delta\phi^{topo}_{t_M t_S}(x,r) = \dfrac{4\pi}{\lambda}\dfrac{B_{\perp t_M t_S}\Delta Z(x,r)}{r\sin\theta} \\ \delta\phi^{disp}_{t_M t_S}(x,r) = \dfrac{4\pi}{\lambda}[d(t_S,x,r) - d(t_M,x,r)] \\ \delta\phi^{atm}_{t_M t_S}(x,r) = \dfrac{4\pi}{\lambda}[d_{atm}(t_S,x,r) - d_{atm}(t_M,x,r)] \end{cases} \quad (1)$$

where λ is the transmitted signal central wavelength, $d(t_S, x, r)$ and $d(t_M, x, r)$ represent the cumulative deformation in the line of sight at times t_S and t_M respectively, with respect to the reference instant t_0, i.e., implying $d(t_0, x, r) = 0$, $\forall (x, r)$; $\Delta Z(x, r)$ is the topographic error present in the DEM used for interferogram generation, and its impact on deformation maps is also a function of the perpendicular baseline component $B_{\perp\, t_M t_S}$, the sensor-target distance r, and the look angle θ. The terms $d_{atm}(t_M, x, r)$ and $d_{atm}(t_S, x, r)$ account for temporal atmospheric variations (and orbital ramps) at pixel (x, r), and the last term $\delta\phi^{noise}_{t_M t_S}(x, r)$ accounts for temporal decorrelation and thermal noise effects.

[12] The displacement term can be expressed as two components: linear and nonlinear displacement:

$$\begin{aligned} \delta\phi^{disp}_{t_M t_S}(x,r) &= \frac{4\pi}{\lambda} v_{mean}(x,r) \times (t_S - t_M) + \sum_{k=M}^{S-1} \delta\phi^{nonlinear}_{k,k+1}(x,r) \\ &= \delta\phi^{linear}_{t_M t_S}(x,r) + \delta\phi^{nonlinear}_{t_M t_S}(x,r) \end{aligned} \quad (2)$$

where v_{mean} is the mean velocity of the given pixel, and $\delta\phi^{nonlinear}_{k,k+1}$ is the nonlinear component between the *kth* and $(k + 1)$*th* time. Equation (1) can hence be expressed as:

$$\begin{aligned} \delta\phi_{t_M t_S}(x,r) = {} & \delta\phi^{topo}_{t_M t_S}(x,r) + \delta\phi^{linear}_{t_M t_S}(x,r) + \delta\phi^{nonlinear}_{t_M t_S}(x,r) \\ & + \delta\phi^{atm}_{t_M t_S}(x,r) + \delta\phi^{noise}_{t_M t_S}(x,r) \end{aligned} \quad (3)$$

The InSAR TS + AEM approach attempts to find a solution for topographic error and the time invariant, constant-rate motion of each pixel, plus a component of nonlinear surface motion (NSM) and the delays associated with atmospheric effects (i.e., Atmospheric Phase Screen, APS) for each scene. For a given set of unwrapped interferograms, the topographic error is correlated with the perpendicular baselines and the mean velocity is through time; therefore the first two terms can be easily estimated and removed from the unwrapped phase (although iteration is used). The main difference between the other three terms is: the nonlinear displacements are correlated both in space and in time, the atmospheric contribution is correlated in space only, while the thermal noise is spatially and temporally decorrelated in the whole set of the unwrapped interferograms. Taking into account the spatial structure of atmospheric effects (e.g., as a power law process [*Williams et al.*, 1998; *Emardson et al.*, 2003; *Li et al.*, 2006]), the APS can be estimated using a temporarily linear velocity (TLV) model [*Li et al.*, 2009] and then distinguished from the NSM. The algorithm is applied iteratively until convergence is achieved. For further details of the InSAR TS + AEM, please refer to *Li et al.* [2009, also manuscript in preparation, 2012] and *Hammond et al.* [2012]. An independent validation with a 10-year GPS data set over the Yucca Mountain suggested that the InSAR TS + AEM derived LOS deformation map using 18 years of ERS and Envisat images agreed with GPS measurements to within 0.5 mm/yr RMS misfit at the stations [*Li et al.*, 2010; *Hammond et al.*, 2012].

3.3. Observed Postseismic Displacement and Validation Map

[13] Figures S3–S8 show the postseismic displacement time series generated by the InSAR TS + AEM method using the five adjacent tracks. It is clear that the postseismic motion appears to be close to linear between 2003 and 2008, which is consistent with the trend in the GPS solution [*Ryder et al.*, 2011]. Because of the lack of InSAR observation during the early postseismic stage (i.e., the first 2 years), it is difficult to determine transient viscosities for this large event, although *Ryder et al.* [2011] used GPS data for the first year to constrain the transient viscosity. As in *Atzori et al.* [2008], we used the cumulative LOS postseismic deformation (instead of the deformation time series) to investigate the postseismic mechanisms of the Kokoxili event and the physical properties of the Tibetan crust. Because the acquisition times of radar images are different for different tracks

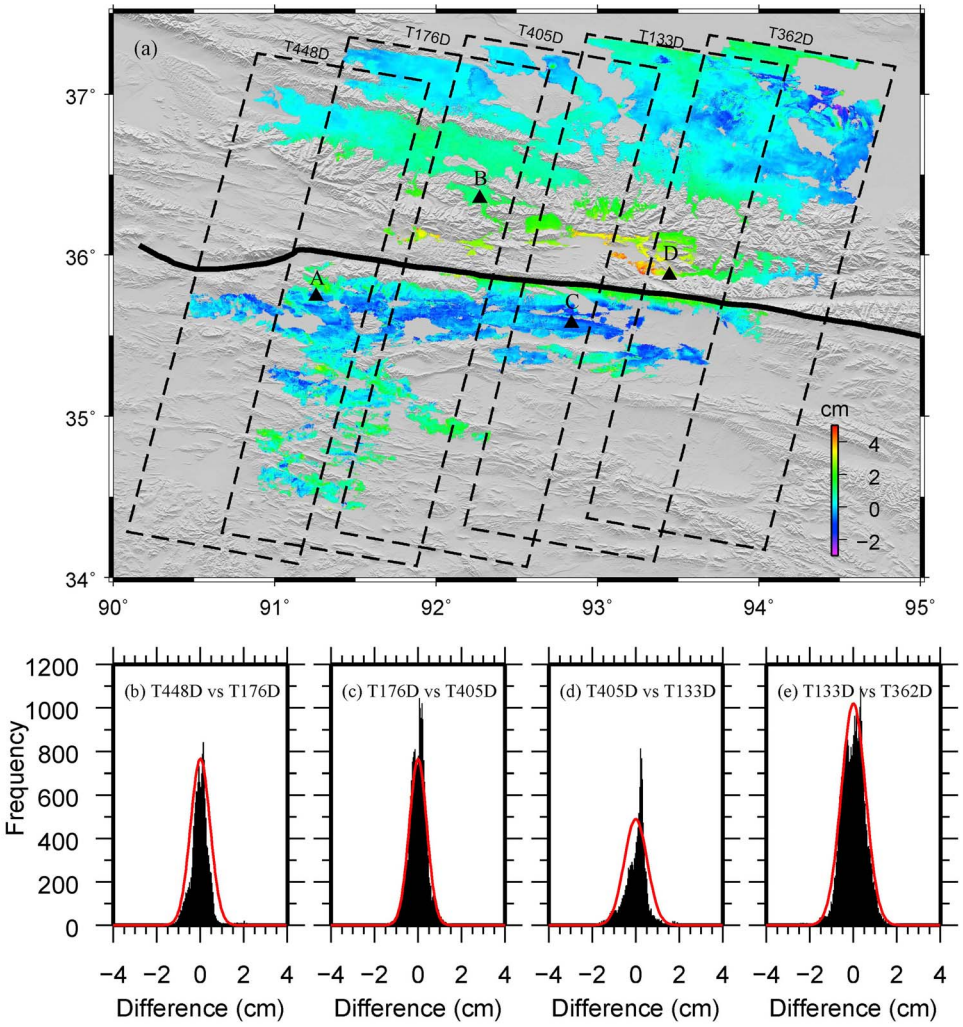

Figure 2. (a) Total cumulative LOS displacement spanning the period between December 2003 and November 2007 (i.e., the common acquisition time period), in cm. Total duration is about 4 yr. Shaded relief SRTM topography is shown in the background. Letters A, B, C and D refer to the sampled points for time series plotting in Figure S8. The LOS displacement differences of common points in the overlapping area between adjacent tracks: (b) Difference between adjacent descending tracks 448 and 176, with a standard derivation of 0.26 cm. (c) Difference between adjacent descending tracks 176 and 405, with a standard derivation of 0.40 cm. (d) Difference between adjacent descending tracks 405 and 133, with a standard derivation of 0.53 cm. (e) Difference between adjacent descending tracks 133 and 362, with a standard derivation of 0.56 cm.

(see Figure S1), a common time interval (December 2003 to November 2007) is selected to calculate the cumulative LOS postseismic deformation for the whole rupture area. A quadratic polynomial function is used to estimate offsets between adjacent tracks based on measurements of overlapping areas. It is clear in Figure 2a that the accumulated LOS surface displacement map shows a pattern with positive LOS range changes to the north of the fault and negative to the south, which for purely horizontal motion is equivalent to left-lateral strike slip. The peak relative displacement occurs in the near field covered by track T133D (at a distance of ∼15 km from both sides of the fault) with a maximum of ∼8 cm range change from peak to trough (track T133D in Figure 2a).

[14] Since there is always an overlap between two adjacent tracks, comparisons between measurements of common areas were performed to assess the consistency of the accumulated LOS surface displacement map (Figures 2b–2e). The standard deviations after an orbital quadratic correction between adjacent tracks range from 0.26 cm to 0.56 cm. Note that the incidence angles vary across the whole image for each track. Assuming that the surface displacements are caused by fault-parallel horizontal movements only, the resultant histograms show similar patterns with similar standard deviations when taking into account the varying incidence angles (Figure S9).

[15] Assuming that the statistical properties of the errors (mainly residual atmospheric effects and orbital ramps) in the accumulated LOS displacement maps have a homogeneous spatial structure across the whole image [*Hanssen*, 2001; *Wright et al.*, 2003; *Parsons et al.*, 2006], 1-D covariance functions can be used to describe the key characteristics

Table 2. The Parameters of 1-D Variance-Covariance Function for the Observed LOS Postseismic Displacements Using a Simple Exponential Function (Equation (4))

Track[a]	Standard Deviation (cm)	e-Folding Length (km)
T448D	0.50	11.4
T176D	0.69	13.0
T405D	0.68	15.3
T133D	0.65	10.0
T362D	0.59	8.6

[a]In the track number, "D" denotes a descending track.

of their uncertainties in each track, including the magnitude and spatial scale. It is found that a simple exponential function provides a good approximation to the observed covariance function [*Parsons et al.*, 2006]:

$$C_{xr} = \sigma^2 e^{-\frac{l}{\alpha}} \quad (4)$$

where C_{xr} is the covariance between pixels x and r with a distance of l, σ^2 is the variance, and α is the e-folding correlation length scale. Table 2 shows a median standard deviation of 0.65 cm with the e-folding wavelength ranging from 8.6 to 15.3 km, which is comparable with previous studies [*Ryder et al.*, 2007; *Li et al.*, 2011].

4. Modeling

[16] The InSAR postseismic map (Figure 2a) consists of hundreds of thousands of data points. In this study, only the deforming parts of the images, extending to about 105 km on either side of the fault, are used in the modeling. Furthermore, the postseismic observations of each track were subsampled individually using a quadtree decomposition algorithm [*Jónsson et al.*, 2002], a technique which concentrates sampling in areas of high phase gradients, thus reducing the number of data points to be modeled from 424261 to 6887.

4.1. Afterslip Modeling

[17] It is clear from Figure 2a that the observed postseismic signal is localized close to the fault of the order of 10–20 km, with a peak-to-trough distance much smaller than the fault length but of the order of the fault locking depth (20–25 km) [*Wang et al.*, 2011], which indicates that the polarity of LOS displacement appears to favor continued slip on the earthquake rupture fault or its extension.

4.1.1. Method

[18] In this study, a kinematic afterslip inversion was performed on rectangular dislocations in an elastic half-space using the formulation of *Okada* [1985]. The fault geometry obtained by *Lasserre et al.* [2005] from the inversion of four adjacent ERS-2 descending coseismic interferograms (Figure 4a) is adopted in the afterslip inversion but with the depth extended down to 50 km. The afterslip fault plane was discretized into 10 km × 10 km patches in the strike and dip direction respectively, and each individual patch was allowed to slip in both dip-slip and positive (left-lateral) strike-slip directions using a Green's function approach:

$$\begin{bmatrix} d \\ 0 \end{bmatrix} = \begin{bmatrix} G & H \\ \kappa^2\nabla^2 & 0 \end{bmatrix} \begin{bmatrix} m \\ t \end{bmatrix} \quad (5)$$

where d is the LOS postseismic displacement, m is the model solution (i.e., slip components on each fault patch), and matrix G is the Green's function relating unit model slip to the predicted displacement. As there are likely to be residual orbital errors in the observed data, H and t were introduced in equation (5) to allow for an additional quadratic polynomial for each track: H is the quadratic ramp matrix and t contains polynomial coefficients. A second-order Laplacian smoothing operator ∇^2 is employed to prevent rough slip distributions [*Jónsson et al.*, 2002], with a balance between the data misfit and the fault slip smoothness controlled by a factor κ that can be derived from a weighted root mean square (wrms) misfit-roughness trade-off curve (Figure 3a). The problem in equation (5) was solved using the Bounded Variable Least Squares (BVLS) algorithm, which also allows constraints to be placed on the sign and/or magnitude of the modeled slip values [*Stark and Parker*, 1995].

[19] While the Kunlun fault is dominantly a vertical left-lateral strike-slip fault, modeling of the rupture with different data sets, e.g., body and surface wave data [*Antolik et al.*, 2004], field measurements [*Xu et al.*, 2006] and InSAR surface displacements [*Lasserre et al.*, 2005], shows a variable component of dip-slip movement along the fault. To allow for a similar variation in the afterslip solution, two components of slip with rakes of 45° and −45° were estimated for each patch, allowing for slip directions up to 45° either side of pure left-lateral strike slip. For each slip patch, the vector sum of these two components gives the total displacement.

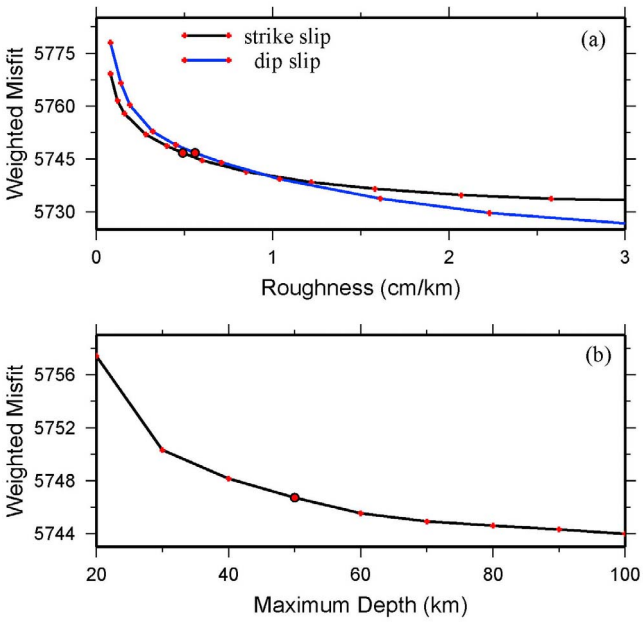

Figure 3. Plot of model misfits for a range of smoothing factors and inversion depths. (a) Trade-off curve between the wrms misfit and the roughness of the slip distribution with a depth extent of 50 km (for both strike and dip slip components). (b) Trade-off curve between the wrms misfit and the maximum slip depth. The red crosses represent the modeled misfits. The red circles represent the value chosen for the inversions presented in Figure 4.

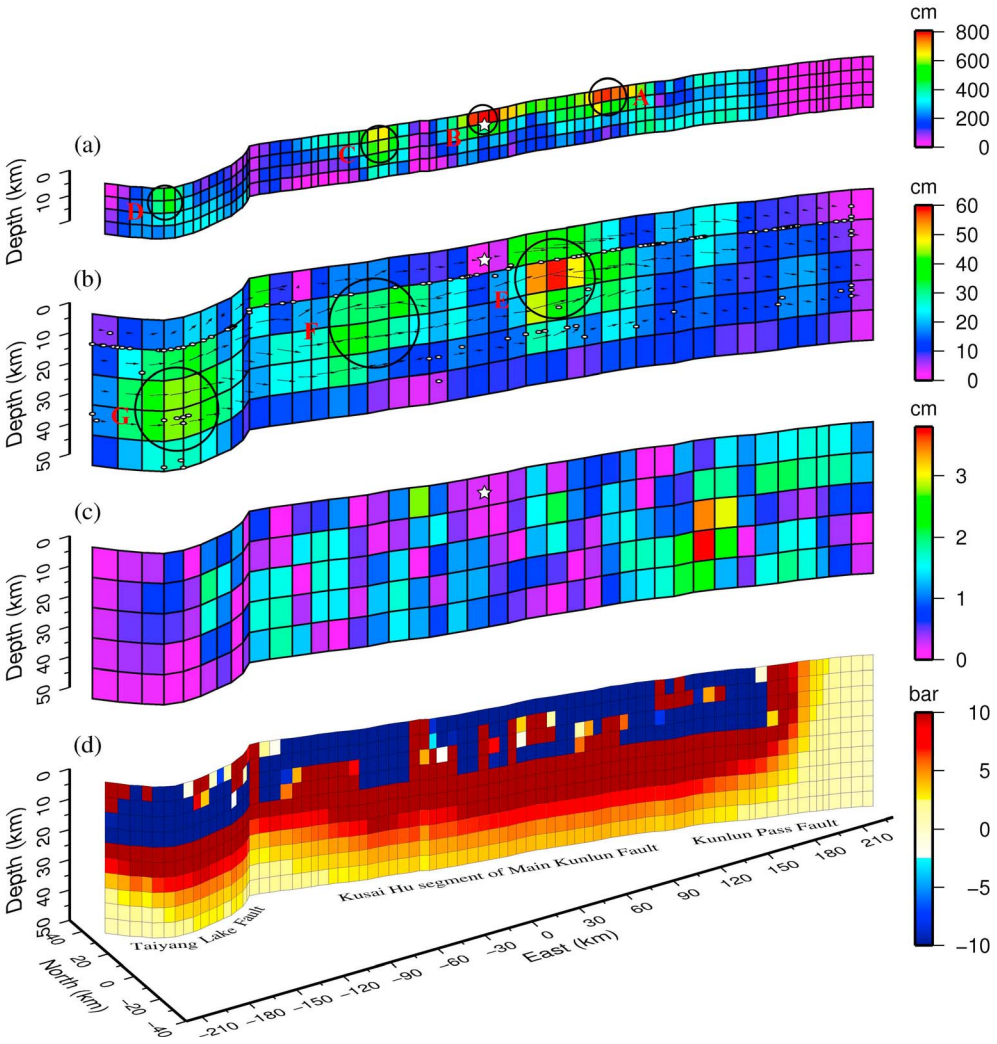

Figure 4. 3D view of coseismic and postseismic slip distribution and model errors. (a) The Kunlun fault geometry and coseismic slip distribution as obtained by *Lasserre et al.* [2005]. The vertical fault is extended to a depth of 20 km and discretized into ~5 km × 5 km patches. The largest slip is about 8 m and occurred at the earthquake epicenter (white star). (b) The postseismic slip distribution from the afterslip model. The depth of the postseismic model is extended to 50 km and discretized into ~10 km × 10 km patches. The white circles represent aftershocks between 14 November 2001 and 31 December 2008. (c) Slip errors on each patch of the fault estimated using a Monte Carlo method. The Monte Carlo errors are an order of magnitude smaller than the estimated slip. (d) Coseismic Coulomb stress changes on the fault plane. The coefficient of the friction is 0.4. Letters A, B, C, D, E, F and G refer to patches mentioned in the text.

[20] To determine to what depth slip should be allowed to occur, a series of inversions was carried out for a range of different depths of the bottom edge of the fault, between 20 km and 100 km [*Ryder et al.*, 2007]. Figure 3b shows the plot of wrms misfit against inversion depth. It is clear that when the allowed depth is shallower than ~40 km, the wrms misfit is large, indicating that the inversion is poor at matching the observations. As the inversion depth increases, the misfit decreases up to the point of the allowed maximum slip depth where the misfit levels off, which is consistent with the finding of *Ryder et al.* [2007] for similar inversions of post-Manyi earthquake afterslip. In the afterslip modeling described below, the maximum inversion depth is fixed to 50 km.

4.1.2. Afterslip Model

[21] The postseismic afterslip distribution from the model inversion is shown in Figure 4b. It is clear that the sense of motion is almost pure left-lateral strike-slip. The InSAR data set has poor spatial coherence in the westernmost tracks, so the afterslip distribution on the Taiyang Lake segment is poorly constrained. A comparison between the coseismic and postseismic slip distributions is shown in Figure 4. The modeled coseismic slip reaches ~ 8 m over the depth range 0~5 km [*Lasserre et al.*, 2005]; the modeled peak postseismic slip is deeper than the maximum coseismic slip, reaching 0.6 m at a depth of 10~20 km. The area with peak slip in both coseismic and postseismic models is located along the central Kusai Hu segment of the main Kunlun

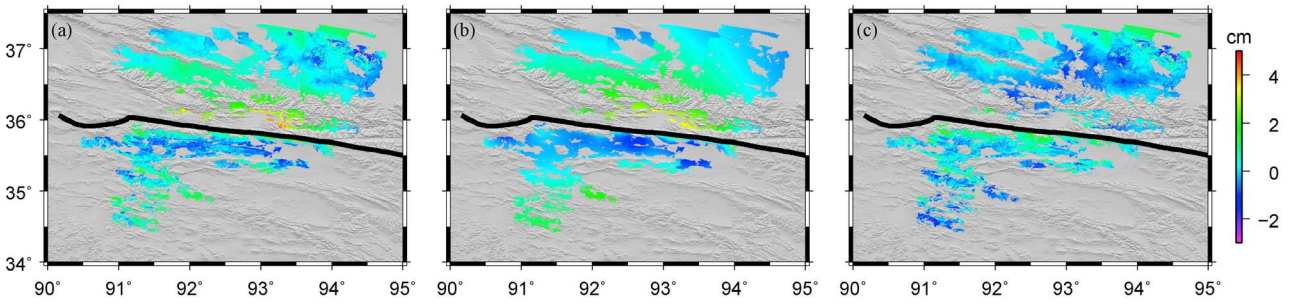

Figure 5. Fit of afterslip model to InSAR range-change field: (a) Observed postseismic map between December 2003 and November 2007, (b) modeled postseismic map, and (c) residual postseismic map with wrms misfit 0.92 cm (rms = 0.73 cm).

fault. The postseismic slip occurred in three patches (patch E, F and G in Figure 4b). The position of the maximum postseismic slip (patch E) is located in between two relatively high coseismic slip patches (patch A and B). There is another area with large slip (patch G) in the postseismic model at the Taiyang Lake fault where the position corresponds to that of the high coseismic slip along the slip zone (patch D). The postseismic slip patch F is located below coseismic patch C.

[22] To investigate the model errors of the afterslip solution, a Monte Carlo method [*Parsons et al.*, 2006] was used in this study. First, one hundred sets of synthetic LOS surface displacements were constructed using the parameterized 1-D covariance function as described in Section 2.3. Second, each set of LOS surface displacements was used to estimate a set of model parameters. Finally, the distributions of the parameters give the model errors (Figure 4c). The Monte Carlo errors are an order of magnitude smaller than the estimated slip, indicating that most of postseismic InSAR data are well explained by the afterslip model.

[23] The predicted LOS postseismic map from the afterslip forward model is shown in Figure 5b, while its corresponding residuals are shown in Figure 5c. The corresponding wrms is 0.92 cm (rms = 0.73 cm). The afterslip model is able to reproduce most of the observed near-field postseismic surface displacements between December 2003 and November 2007, with the large residual values observed far from the fault trace.

4.2. Viscoelastic Model

[24] Models of viscoelastic relaxation in the lower crust and upper mantle were also used to explore the source of the observed postseismic displacements. Any earthquake-induced stress changes occurring within viscoelastic material in the crust or upper mantle will be relaxed by viscous flow, with the time constant of stress relaxation governed by the viscosity. *Ryder et al.* [2011] reported that both Maxwell and Burgers rheology produce similar spatial patterns of postseismic deformation. In this study, due to the lack of InSAR observations in the early postseismic stage (i.e., the first 2 years), a Maxwell rheology is chosen for this exercise rather than the Burgers rheology as in *Ryder et al.* [2011].

4.2.1. Method

[25] In this study, the PSGRN/PSCMP program [*Wang et al.*, 2006] was employed to simulate the LOS surface displacements resulting from the stresses imposed by the 2001 Kokoxili earthquake on viscoelastic layered rheologies. The PSGRN/PSCMP code solves a linear viscoelastic boundary-value problem adopting the associated elastic solutions in which the elastic moduli are replaced by the Laplace or Fourier transformed complex moduli, which has been successfully applied in several previous studies [e.g., *Lorenzo-Martín et al.*, 2006; *Fay et al.*, 2008]. The difference between deformation signals computed with spherical models [e.g., *Pollitz*, 1992] and the plane-earth model of PSGRN/PSCMP should not be larger than a few percent even for the largest earthquake with a spatial extension of 3000 km [*Wang et al.*, 2006]. The displacements calculated by PSGRN/PSCMP are accurate enough for this case. In this study, the coseismic parameters are obtained from the slip model of *Lasserre et al.* [2005], which is based on an inversion of 4 adjacent tracks of InSAR images.

[26] To model the stress relaxation with a Maxwell rheology, a three-layered rheology model (here referred to as the three-layer model, Figure 6) is used to investigate a range of viscosities. For these models, the elastic properties of the model domain are constant throughout (shear modulus of 40 GPa, Poisson's ratio of 0.25). The upper layer is an elastic lid whose thickness is fixed at 15 km, which is consistent with the depth above which most coseismic slip occurred [*Lasserre et al.*, 2005]. The second layer is viscoelastic and corresponds to the lower crust with viscosities ranging between 1×10^{17} Pa s (weak crust) and 1×10^{29} Pa s (essentially elastic), as in the Denali study of *Biggs et al.* [2009]. From the observations of teleseismic shear-coupled P waves, *Owens and Zandt* [1997] inferred that the crustal thickness of the Songpan-Ganzi terrane is 55 km. *Zhu and Helmberger* [1998] suggested a crustal thickness of ~70 km beneath the Kunlun mountains based on broadband teleseismic body waves. Using gravity data, *Braitenberg et al.* [2003] reported the same thickness in the Qaidam basin. Analyzing a wide-angle reflection and refraction profile collected across the NE Tibetan Plateau and the Himalaya, *Karplus et al.* [2011] estimated a crustal thickness of 70 km beneath the Songpan terrane and East Kunlun Mountains. Therefore, the base of the crust is fixed at 70 km in this study. The final layer is a viscoelastic half-space corresponding to the upper mantle with a range of viscosities, 1×10^{17} Pa s $< \eta_{um} < 1 \times 10^{21}$ Pa s [e.g., *Ryder et al.*, 2007; *Biggs et al.*, 2009]. For each rheological structure, the

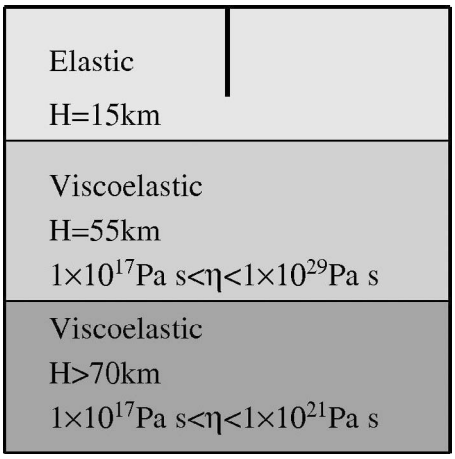

Figure 6. Cross-section of three-layer viscoelastic earth model. The model is composed of a Maxwell viscoelastic layer sandwiched between an elastic lid and Maxwell viscoelastic half-space. The material parameters of the viscoelastic lower crust and half-space are varied. The thicknesses (H) of the elastic lid and the viscoelastic sandwich are fixed to 15 and 55 km, respectively.

residual between modeled and observed InSAR line-of-sight displacement is calculated, and a best fitting quadratic function for each track is estimated, which is used to remove any remaining orbital error. Each forward model is then compared to its corresponding InSAR observations, to calculate the wrms misfit.

4.2.2. Viscoelastic Results

[27] Figure 7 shows the fit of modeled surface line-of-sight displacements from 2003 to 2007 as a function of lower-crust and upper-mantle viscosity. The modeled displacements are not very sensitive to the rheology of the mantle below the Tibetan crust and we find two domains of upper mantle viscosities (η_{um}) (a low viscosity domain ($<2 \times 10^{17}$ Pa s) and high domain ($\eta_{um} > 2 \times 10^{18}$ Pa s)), with slightly lower misfits. The forward-modeled surface line-of-sight displacements from the best fitting model with both lower crustal and upper mantle viscosities of 2×10^{19} Pa s are shown in Figure 8. The corresponding wrms misfit is 0.93 cm (rms = 0.81 cm). It is clear that the simulated displacement field has smaller amplitude than the observed InSAR displacement field. Furthermore, none of the viscoelastic simulations show strain accumulation as close to the fault as seen in the InSAR result, which indicates that the viscoelastic model cannot match displacements both close to and away from the fault.

4.3. Mixed Mechanism

[28] *Shen et al.* [2003] modeled the GPS postseismic deformation following the Kokoxili earthquake using a combination of mechanisms, with viscoelastic relaxation in the lower crust and afterslip on the downdip side of the coseismic rupture zone. We also consider the possibility that both mechanisms occur, but in spatially distinct areas: afterslip in the crust and viscoelastic relaxation in the mid-to-lower crust and uppermost mantle during the postseismic period.

[29] To model this, the displacements caused by relaxation of a viscoelastic half-space below an elastic lid are calculated using PSGRN/PSCMP software [*Wang et al.*, 2006]. These estimates are removed from the InSAR line-of-sight data, and a linear inversion as in the previous afterslip modeling is used to find any additional afterslip in the crust, as in *Biggs et al.* [2009]. For these models, the maximum afterslip depth of 50 km is chosen and the viscosity of the viscoelastic half-space is fixed to 2×10^{19} Pa s determined in the previous sections. Three values of thickness of the elastic lid including 15 km (the upper crustal thickness), 50 km (the middle crustal thickness) and 70 km (the lower crustal thickness) are used to investigate the trade-off between afterslip and viscoelastic relaxation mechanisms.

[30] In these cases, any observed LOS displacements which are not reproduced by the viscoelastic model can be

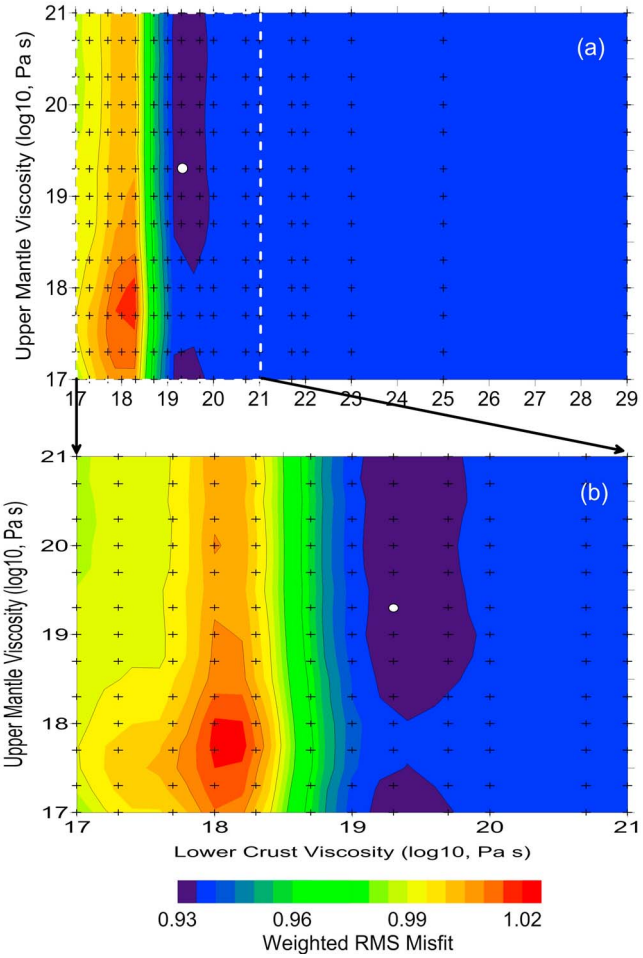

Figure 7. (a) Plot of weighed misfit (normalized) for a range of viscoelastic forward models composed of viscoelastic lower crust of viscosity η_{lc}, overlying a viscoleastic half-space (upper mantle) with viscosity η_{um}. (b) Enlarged lower crust viscosity segment of the white box in Figure 7a. A quadratic ramp for each track is estimated from the residual and removed from observed line-of-sight postseismic displacements to adjust for any remaining orbital error. The black crosses represent the results of modeled wrms, which are interpolated onto a regular grid. The white circle represents the value chosen for the inversions presented in Figure 8.

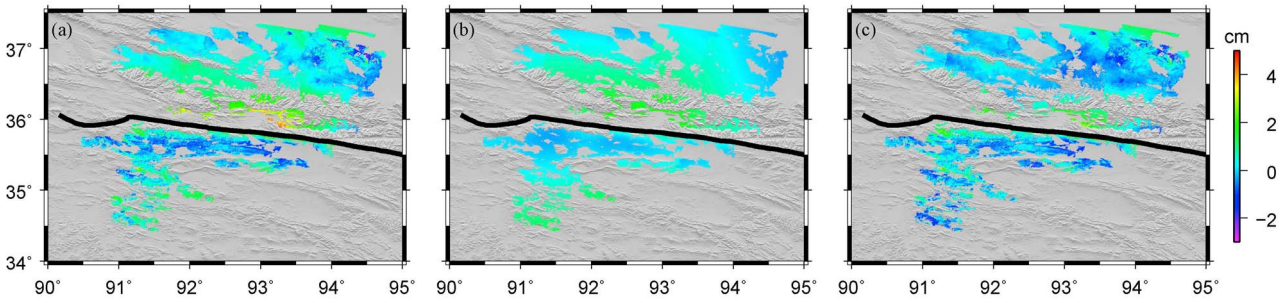

Figure 8. (a) Observed, (b) simulated and (c) residual line-of-sight displacement from viscoelastic relaxation model with $\eta_{lc} = 2 \times 10^{19}$ Pa s and $\eta_{um} = 2 \times 10^{19}$ Pa s. The corresponding wrms misfit is 0.93 cm (rms = 0.81 cm).

attributed to afterslip. Figure 9 shows the afterslip distributions for the mixed models with different elastic lid thicknesses (15 km, 50 km and 70 km) and a viscosity of 2×10^{19} Pa s. In general, the average afterslip in each case is about 16 cm. The maximum slips are 49, 54 and 57 cm respectively, which are located at the same location as the peak slip in the previous afterslip inversion. The corresponding wrms misfits are 0.94 cm (rms = 0.78 cm), 0.93 cm (rms = 0.71 cm) and 0.93 cm (rms = 0.69 cm), respectively. There is no significant difference between the wrms misfits for the 15 km and >50 km elastic lid models, although lower wrms misfits are found for thicker-lid models. This may indicate that the afterslip model could fit the near-fault surface displacements better than the model of viscoelastic relaxation in the mid-to-lower crust.

5. Discussion

[31] Postseismic motion for large strike-slip earthquakes is likely to be caused by poroelastic rebound, afterslip, viscoelastic relaxation or a combination of these end-member models (e.g., Table 3). Poroelastic rebound is expected to be restricted both spatially and temporally [e.g., *Peltzer et al.*, 1998; *Jónsson et al.*, 2003; *Freed et al.*, 2006a, 2006b; *Biggs et al.*, 2009]. The displacements caused by poroelastic rebound are likely to take place within a few kilometers of the fault and would be reached within a few months of the earthquake. Since the observed InSAR line-of-sight displacements presented here are at much greater distances and over longer time periods (2–6 yr after the earthquake), poroelastic rebound is unlikely to have a significant effect and is not considered further in this study.

[32] Afterslip and viscoelastic relaxation models are employed to explore the source of the observed postseismic deformation following the 2001 Kokoxili earthquake during the time period between 2 and 6 years after the event. It appears that the observed displacements do not clearly favor either afterslip or viscoelastic relaxation because of the similar weighted RMS misfits, which highlights the fact that different mechanisms can reproduce very similar spatial patterns of displacement at the surface [e.g., *Hearn*, 2003] (Figures 5 and 8). In previous studies, the pattern of vertical displacement, to which InSAR is particularly sensitive, has been used to distinguish between afterslip and viscoelasic relaxation mechanisms for the case of the 1999 Hector Mine event [*Pollitz et al.*, 2001]. However, in this study, both models are capable of providing a satisfactory fit to the observed single line-of-sight displacements, which is similar to results from studies of postseismic deformation following the Manyi [*Ryder et al.*, 2007] and Denali events [*Biggs et al.*, 2009]. Furthermore, there is only a very small amount of ascending SAR data for this event, so it is not possible to distinguish between these two possibilities using the postseismic line-of-sight surface displacements data from the Kokoxili earthquake.

[33] The result of the afterslip inversion suggests that aseismic slip is a possible mechanism to explain the observed line-of-sight surface displacements. Our model has about three times the 18 cm maximum afterslip estimated by *Ryder et al.* [2011], which can be attributed to the data used in the afterslip inversions covering different time intervals. In *Ryder et al.* [2011], the afterslip was modeled for a ~1-year observation period (December 2003 - December 2004), which is different from the data spanning two to six years after the earthquake used in this study. Although the inversion results are purely kinematic, the maximum slip occurred on the Kusai segment, in the middle of two relatively high coseismic slip patches, and the afterslip in general occurs well below the coseismic rupture. Apart from the localized residuals, the major part of the postseismic LOS displacement is well explained by the afterslip model. The afterslip located in the Taiyang Lake fault (patch G) may result from the residual orbit effect; note that it is difficult to separate orbital parameters from long-wavelength displacements in current InSAR observations. The simple afterslip model in this study is not capable of distinguishing lower crustal deformation occurring in a broad or a narrow shear zone [e.g., *Bürgmann and Dresen*, 2008].

[34] In this study, Coulomb stress changes resulting from the Kokoxili rupture are calculated using the Coulomb 3.3 software [*Toda et al.*, 2005]. The coseismic slip distribution of *Lasserre et al.* [2005] is used as the source. The stress changes are calculated for a "fixed" receiver fault using the same geometry and kinematics as the coseismic fault, except that the downdip width extends to 50 km. The effective coefficient of friction in calculations is given a value of 0.4, which is considered appropriate for mature faults [*Harris*, 1998]. A comparison between the postseismic slip distributions and Coulomb stress changes (Figures 4c and 4d) shows that most of the afterslip occurred where the stress changes

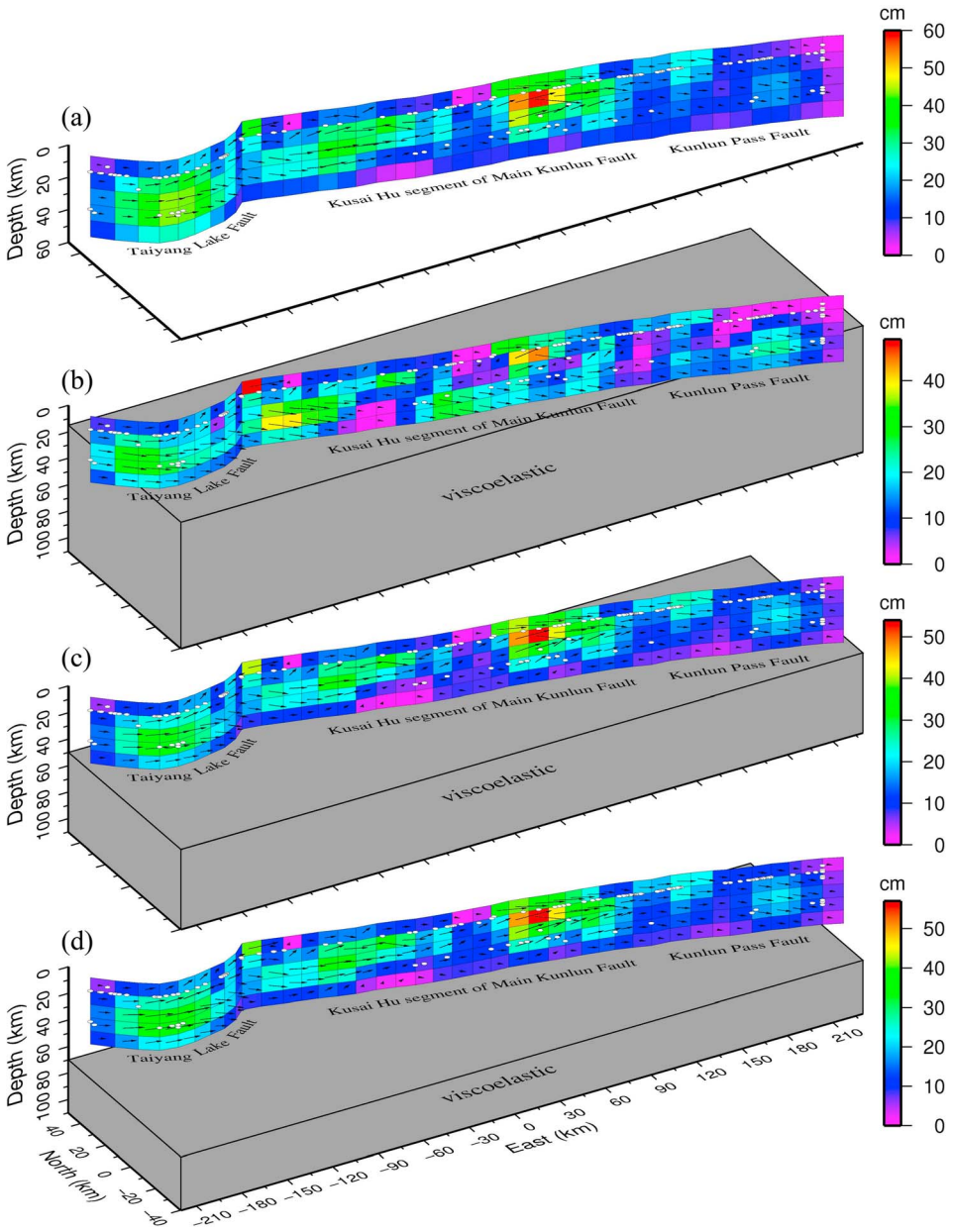

Figure 9. Mixed mechanism models for postseismic displacement with afterslip in the crust and viscoelastic relaxation in the mid-to-lower crust and uppermost mantle. (a) The afterslip distribution as shown in Figure 4b. The viscoelastic models have different values of elastic lid thickness ((b) 15 km, (c) 50 km, and (d) 70 km) over a half-space with viscosity 2×10^{19} Pa s.

were positive. Spatial correlations between the changes in Coulomb stress and location of postseismic slip are evident. This is consistent with a stress-driven afterslip model in which stress increases from the earthquake are later released aseismically [*Freed et al.*, 2006a; *Johanson et al.*, 2006; *Hearn et al.*, 2009].

[35] From the results of the viscoelastic model, we find that the most of the postseismic surface displacement during 2003–2007 is due to relaxation in both the lower crust and the upper mantle. In some strike-slip earthquakes, such as Izmit, Turkey [*Hearn et al.*, 2002] and Manyi, Tibet [*Ryder et al.*, 2007], the lower crust has been the major zone of relaxation, while in other events (Landers, Hector Mine, California) upper mantle deformation was found to be important [*Pollitz et al.*, 2001; *Freed and Bürgmann*, 2004]. In the Kokoxili case, the modeled displacements are not sensitive to the upper mantle viscosity, indicating that viscoelastic relaxation occurs dominantly from the middle crust to the lower crust, which is due to the great crustal thickness and limited extent and precision of the far-field InSAR data.

[36] If the rheology is nonlinear, transient or both, the effective viscosity may be stress- and time-dependent [*Freed et al.*, 2006b]. Analysis of the postseismic response to the 1997 Manyi, Tibet earthquake [*Ryder et al.*, 2007] shows that the effective Maxwell viscosity may change by a factor of three during the first 3–4 years after an earthquake, with

Table 3. Mechanisms of Postseismic Deformation for Large Strike-Slip Earthquakes

Event	Mechanism	Source
Denali earthquake	viscoelastic relaxation/afterslip/combination	*Biggs et al.* [2009]
	afterslip and viscoelastic relaxation	*Johnson et al.* [2009]
	viscoelastic relaxation/afterslip/combination	*Freed et al.* [2006a]
Manyi earthquake	viscoelastic relaxation/afterslip	*Ryder et al.* [2007]
Kokoxili earthquake	afterslip and viscoelastic relaxation	*Shen et al.* [2003]
	viscoelastic relaxation/afterslip	*Ryder et al.* [2011]
	viscoelastic relaxation/afterslip/combination	This study
Landers earthquake	poroelastic rebound and afterslip	*Fialko* [2004]
	viscoelastic relaxation	*Pollitz et al.* [2000]
	poroelastic rebound	*Peltzer et al.* [1998]
Landers and Hector Mine earthquake	viscoelastic relaxation	*Freed and Bürgmann* [2004]
Izmit earthquake	afterslip	*Bürgmann et al.* [2002]
	afterslip	*Hearn et al.* [2002]
	afterslip and viscoelastic relaxation	*Hearn et al.* [2009]
Siberian Altai earthquake	viscoelastic relaxation/afterslip	*Barbot et al.* [2008]

values of $\sim$3–10 $\times$ 10^{18} Pa s. An increase in viscosity is also suggested by studies of rheological properties beneath Tibet using GPS and leveling data, where the effective viscosity during 7–26 years after the Luhuo earthquake on the central segment of Xianshuihe fault is 2 orders of magnitude larger than in the first year after the Kokoxili event in northern Tibet [*Zhang et al.*, 2009]. Considering the inferred increase of effective viscosities for later postseismic observation periods in these previous studies, our preferred viscoelastic relaxation model for the Kokoxili event is consistent with results of *Ryder et al.* [2007] and *Zhang et al.* [2009].

[37] The estimated rheological properties beneath Tibet using different methods range from $10^{16}\sim10^{21}$ Pa s (see Table 4). Several modeling studies of the present-day topography of Tibet argued for a weak middle and/or lower crust beneath the plateau as a whole, with viscosities ranging from $10^{16}\sim10^{20}$ Pa s [*Royden*, 1996; *Clark and Royden*, 2000; *Beaumont et al.*, 2001; *Medvedev and Beaumont*, 2001]. *Hilley et al.* [2009] used GPS surface velocities to estimate a crustal viscosity of $\geq10^{18}$ Pa s for northern Tibet in a model taking into account time-dependent earthquake cycle effects. *Ryder et al.* [2010] considered InSAR data covering the 2008 Nima-Gaize earthquake to place a strong lower bound of 3 $\times$ 10^{17} Pa s on the viscosity of the mid to lower crust of central Tibet. Using GPS time series (first year) and InSAR LOS measurements for the Kokoxili earthquake, *Ryder et al.* [2011] inferred a transient viscosity of 9 $\times$ 10^{17} Pa s and a steady state viscosity of 1 $\times$ 10^{19} Pa s in northeastern Tibet. Our estimate of 2 $\times$ 10^{19} Pa s from the Kokoxili earthquake after 2–6 years may be the steady lower crust to upper mantle viscosity for this part of Tibet, which is consistent with the values from the InSAR time series of *Ryder et al.* [2007, 2011].

6. Conclusions

[38] This study has shown that significant postseismic motion occurred in years 2 to 6 following the 2001 Kokoxili earthquake. Using multitemporal SAR interferometry, the LOS displacement field has revealed up to 8 cm of peak to trough deformation occurring at $\sim$15 km from the fault trace. The observed surface displacements can be modeled by afterslip on a discrete fault plane or relaxation of a Maxwell viscoelastic medium or a combination of both. The inversion for afterslip on a deep extension of the coseismic fault plane at depth gives a slip distribution whose high slip patches are adjacent to areas of high coseismic slip, suggesting that this is a feasible process. The afterslip modeling gives a maximum of 60 cm of strike slip during the 2–6 years after the earthquake. Modeling of viscoelastic relaxation in a Maxwell half-space, and also a mixed mechanism model, enables us to place an effective viscosity of 2 $\times$ 10^{19} Pa s on the lower crust to mantle of northern Tibet. Integration with a dense network of GPS stations and SAR

Table 4. Viscosities Estimated From Different Studies in Tibet

Event/Data	Data	Time	Depth	Viscosity (Pa s)	Source
Kokoxili earthquake	InSAR	Post 2–6 years	>15 km	2 $\times$ 10^{19}	This study
	GPS + InSAR	Transient	16.5–81.5 km	9 $\times$ 10^{17}	*Ryder et al.* [2011]
		Steady state		1 $\times$ 10^{19}	
	GPS	Post 6 months	Lower crust	5 $\times$ 10^{17}	*Shen et al.* [2003]
	GPS	Short-term	Middle to lower crust and mantle	$\geq10^{18}$	*Hilley et al.* [2009]
	GPS	Post 1 year	Lower crust	10^{17}	*Zhang et al.* [2009]
	Fault slip	Long-term	Mid-crust	10^{19}-2 $\times$ 10^{21}	*Hilley et al.* [2005]
Nima-Gaize earthquake	InSAR	Post 9 months	>14 km	3 $\times$ 10^{17}	*Ryder et al.* [2010]
Luhuo earthquake	Leveling	Post 7–30 years	>31 km	10^{19}-10^{21}	*Zhang et al.* [2009]
Manyi earthquake	InSAR	Post 25 days	>15 km	4 $\times$ 10^{18}	*Ryder et al.* [2007]
		Post 1145 days		10^{19}	
Plateau	Topography + GPS	–	Lower crust	$\geq10^{19}$	*Cook and Royden* [2008]
	Topography	–	Middle to lower crust	10^{18}-10^{19}	*Beaumont et al.* [2001]
	Topography	–	Lower crust	10^{16}	*Medvedev and Beaumont* [2001]
	Relief	–	Lower crust	10^{18}-10^{21}	*Royden* [1996]

tracks (descending and ascending tracks) might enable mechanisms of postseismic motion to be distinguished.

[39] **Acknowledgments.** This work was supported by the National Natural Science Foundation of China (40874003 and 41074007), the National Department Public Benefit Research Foundation (Earthquake) (200808080) and the National High Technology Research and Development Program of China (863 Program) (2009AA12Z317), the Research Fund for the Doctoral Program of Higher Education of China (20090141110055 and 20100141120033) and the Fundamental Research Funds for the Central Universities (114035 and 3101036). Part of this work was carried out in the University of Glasgow, which was supported by the Natural Environmental Research Council (NERC) through the GAS project (Ref: NE/H001085/1). We thank Juliet Biggs and Eric Fielding for their incisive comments. We are very grateful to C. Lasserre for providing her coseismic slip distribution of the 2001 Kokoxili event. The ENVISAT images were supplied through the ESA-MOST Dragon 2 Cooperation Program (ID: 5343) and the C1P.336 project. Most of figures were prepared using the GMT mapping software [*Wessel and Smith*, 1998].

References

Antolik, M., R. E. Abercrombie, and G. Ekström (2004), The 14 November, 2001 Kokoxili (Kunlunshan), Tibet, earthquake: Rupture transfer through a large extensional step-over, *Bull. Seismol. Soc. Am.*, *94*(4), 1173–1194, doi:10.1785/012003180.

Atzori, S., et al. (2008), Postseismic displacement of the 1999 Athens earthquake retrieved by the Differential Interferometry by Synthetic Aperture Radar time series, *J. Geophys. Res.*, *113*, B09309, doi:10.1029/2007JB005504.

Barbot, S., Y. Hamiel, and Y. Fialko (2008), Space geodetic investigation of the coseismic and postseismic deformation due to the 2003 M_w 7.2 Altai earthquake: Implications for the local lithospheric rheology, *J. Geophys. Res.*, *113*, B03403, doi:10.1029/2007JB005063.

Beaumont, C., et al. (2001), Himalayan tectonics explained extrusion of low-viscosity crustal channel coupled to focused surface denudation, *Nature*, *414*, 738–742, doi:10.1038/414738a.

Berardino, P., et al. (2002), A new algorithm for surface deformation monitoring based on small baseline differential SAR interferograms, *IEEE Trans. Geosci. Remote Sens.*, *40*, 2375–2383, doi:10.1109/TGRS.2002.803792.

Biggs, J., et al. (2007), Multi-interferogram method for measuring interseismic deformation: Denali Fault, Alaska, *Geophys. J. Int.*, *170*, 1165–1179, doi:10.1111/j.1365-246X.2007.03415.x.

Biggs, J., et al. (2009), The postseismic response to the 2002 M 7.9 Denali Fault earthquake: Constraints from InSAR 2003–2005, *Geophys. J. Int.*, *176*, 353–367, doi:10.1111/j.1365-246X.2008.03932.x.

Braitenberg, C., et al. (2003), Spatial variations of flexure parameters over the Tibet-Quinghai plateau, *Earth Planet. Sci. Lett.*, *205*(3–4), 211–224, doi:10.1016/S0012-821X(02)01042-7.

Bufe, C. G. (2004), Comparing the November 2002 Denali and November 2001 Kunlun earthquake, *Bull. Seismol. Soc. Am.*, *94*(3), 1159–1165, doi:10.1785/0120030185.

Bürgmann, R., and G. Dresen (2008), Rheology of the lower crust and upper mantle: Evidence from rock mechanism, geodesy and field observations, *Annu. Rev. Earth. Planet. Sci.*, *36*, 531–567, doi:10.1146/annurev.earth.36.031207.124326.

Bürgmann, R., P. Rosen, and E. Fielding (2000), Synthetic aperture radar interferometry to measure Earth's surface topography and its deformation, *Annu. Rev. Earth Planet. Sci.*, *28*, 169–209, doi:10.1146/annurev.earth.28.1.169.

Bürgmann, R., et al. (2002), Time-space variable afterslip on and deep below the Izmit earthquake rupture, *Bull. Seismol. Soc. Am.*, *92*, 126–137, doi:10.1785/0120000833.

Chen, C. W., and H. A. Zebker (2002), Phase unwrapping for large SAR interferograms: Statistical segmentation and generalized network models, *IEEE Trans. Geosci. Remote Sens.*, *40*, 1709–1719, doi:10.1109/TGRS.2002.802453.

Clark, M. K., and L. H. Royden (2000), Topographic ooze: Building the eastern margin of Tibet by lower crustal flow, *Geology*, *28*, 703–706.

Cook, K. L., and L. H. Royden (2008), The role of crustal strength variations in shaping orogenic plateaus, with application to Tibet, *J. Geophys. Res.*, *113*, B08407, doi:10.1029/2007JB005457.

Division of Earthquake Monitoring and Prediction (1995), *Catalogue of Chinese Historical Strong Earthquake* [in Chinese], Seismol. Press, Beijing.

Division of Earthquake Monitoring and Prediction (1999), *Catalogue of Chinese Modern Earthquakes* [in Chinese], Sci. and Technol. Press, Beijing.

Emardson, T. R., M. Simons, and F. H. Webb (2003), Neutral atmospheric delay in interferometric synthetic aperture radar applications: Statistical description and mitigation, *J. Geophys. Res.*, *108*(B5), 2231, doi:10.1029/2002JB001781.

Farr, M., et al. (2007), The Shuttle Radar Topography Mission, *Rev. Geophys.*, *45*, RG2004, doi:10.1029/2005RG000183.

Fay, N. P., R. A. Bennett, and S. Hreinsdóttir (2008), Contemporary vertical velocity of central Basin and Range and uplift of the southern Sierra Nevada, *Geophys. Res. Lett.*, *35*, L20309, doi:10.1029/2008GL034949.

Fialko, Y. (2004), Evidence of fluid-filled upper crust from observations of postseismic deformation due to the 1992 M_w7.3 Landers earthquake, *J. Geophys. Res.*, *109*, B08401, doi:10.1029/2004JB002985.

Fitch, T. J. (1970), Earthquake mechanism in the Himalayan, Burmese and Adaman regions and continental tectonics in central Asia, *J. Geophys. Res.*, *75*, 2699–2709, doi:10.1029/JB075i014p02699.

Freed, A. M., and R. Bürgmann (2004), Evidence of power-law flow in the Mojave desert mantle, *Nature*, *430*, 548–551, doi:10.1038/nature02784.

Freed, A., et al. (2006a), Implications of deformation following the 2002 Denali, Alaska, earthquake for postseismic relaxation processes and lithospheric rheology, *J. Geophys. Res.*, *111*, B01401, doi:10.1029/2005JB003894.

Freed, A. R., et al. (2006b), Stress-dependent power-law flow in the upper mantle following the 2002 Denali, Alaska, earthquake, *Earth Planet. Sci. Lett.*, *252*, 481–489, doi:10.1016/j.epsl.2006.10.011.

Funning, G. J., B. Parsons, and T. J. Wright (2007), Fault slip in the 1997 Manyi, Tibet earthquake from linear elastic modeling of InSAR displacements, *Geophys. J. Int.*, *169*, 988–1008, doi:10.1111/j.1365-246X.2006.03318.x.

Gan, W., et al. (2007), Present-day crustal motion within the Tibetan Plateau inferred from GPS measurements, *J. Geophys. Res.*, *112*, B08416, doi:10.1029/2005JB004120.

Goldstein, R. M., and C. L. Werner (1998), Radar interferogram filtering for geophysical applications, *Geophys. Res. Lett.*, *25*, 4035–4038, doi:10.1029/1998GL900033.

Hammond, W. C., G. Blewitt, Z. Li, H.-P. Plag, and C. W. Kreemer (2012), Contemporary uplift of the Sierra Nevada, western United States from GPS and InSAR measurements, *Geology*, doi:10.1130/G32968.1, in press.

Hanssen, R. (2001), *Radar Interferometry—Data Interpretation and Error Analysis*, *Remote Sens. and Digital Image Processing*, vol. 2, Kluwer Acad., Dordrecht, Netherlands.

Harris, R. A. (1998), Introduction to special section: Stress triggers, stress shadows, and implications for seismic hazard, *J. Geophys. Res.*, *103*(B10), 24,347–24,358, doi:10.1029/98JB01576.

Hearn, E. H. (2003), What can GPS data tell us about the dynamics of postseismic deformation?, *Geophys. J. Int.*, *155*, 753–777, doi:10.1111/j.1365-246X.2003.02030.x.

Hearn, E., R. Bürgmann, and R. Reillinger (2002), Dynamic of Izmit earthquake postseismic deformation and loading of the Duzce earthquake epicenter, *Bull. Seismol. Soc. Am.*, *92*, 172–193, doi:10.1785/0120000832.

Hearn, E. H., et al. (2009), Izmit earthquake postseismic deformation and dynamics of the North Anatolian Fault Zone, *J. Geophys. Res.*, *114*, B08405, doi:10.1029/2008JB006026.

Hilley, G. E., et al. (2005), Bayesian inference of plastosphere viscosities near the Kunlun Fault, northern Tibet, *Geophys. Res. Lett.*, *32*, L01302, doi:10.1029/2004GL021658.

Hilley, G. E., et al. (2009), Earthquake-cycle deformation and fault slip rates in northern Tibet, *Geology*, *37*, 31–34, doi:10.1130/G25157A.1.

Jia, Y., H. Dai, and X. Su (1988), Tuosuo Lake earthquake fault in Qinghai province, in *Research on Earthquake Faults in China*, pp. 66–71, Xingjiang Press, Xingjiang, China.

Johanson, I. A., et al. (2006), Coseismic and postseismic slip of the 2004 Parkfield earthquake from space-geodetic data, *Bull. Seismol. Soc. Am.*, *96*(4B), S269–S282, doi:10.1785/0120050818.

Johnson, K. M., R. Bürgmann, and J. Freymuller (2009), Coupling afterslip and viscoelastic flow following the 2002 Denali Fault, Alaska earthquake, *Geophys. J. Int.*, *176*, 670–682, doi:10.1111/j.1365-246X.2008.04029.x.

Jónsson, S., et al. (2002), Fault slip distribution of the 1999 Mw 7.2 Hector Mine earthquake, California, estimated from satellite radar and GPS measurements, *Bull. Seismol. Soc. Am.*, *92*(4), 1377–1389, doi:10.1785/0120000922.

Jónsson, S., et al. (2003), Post-earthquake ground movements correlated to pore-pressure transient, *Nature*, *424*, 179–183, doi:10.1038/nature01776.

Karplus, M. S., et al. (2011), Injection of Tibetan crust beneath the south Qaidam Basin: Evidence from INDEPTH IV wide-angle seismic data, *J. Geophys. Res.*, *116*, B07301, doi:10.1029/2010JB007911.

Kirby, E., et al. (2007), Slip rate gradients along the eastern Kunlun fault, *Tectonics*, *26*, TC2010, doi:10.1029/2006TC002033.

Klinger, Y. R., R. Michel, and G. King (2006), Evidence for a barrier model from Mw 7.8 Kokoxili (Tibet) earthquake slip-distribution, *Earth Planet. Sci. Lett.*, *242*, 354–364, doi:10.1016/j.epsl.2005.12.003.

Lasserre, C., et al. (2005), Coseismic deformation of the 2001 Mw = 7.8 Kokoxili earthquake in Tibet, measured by synthetic aperture radar interferometry, *J. Geophys. Res.*, *110*, B12408, doi:10.1029/2004JB003500.

Li, H., et al. (2005), Slip rate on the Kunlun fault at Hongshui Gou, and recurrence time of great events comparable to the 14/11/2001, Mw 7.9 Kokoxili earthquake, *Earth Planet. Sci. Lett.*, *237*, 285–299, doi:10.1016/j.epsl.2005.05.041.

Li, Z., et al. (2006), Interferometric synthetic aperture radar atmospheric correction: GPS topography-dependent turbulence model, *J. Geophys. Res.*, *111*, B02404, doi:10.1029/2005JB003711.

Li, Z., E. J. Fielding, and P. Cross (2009), Integration of InSAR time series analysis and water vapour correction for mapping postseismic deformation after the 2003 Bam, Iran earthquake, *IEEE Trans. Geosci. Remote Sens.*, *47*(9), 3220–3230, doi:10.1109/TGRS.2009.2019125.

Li, Z., W. C. Hammond, G. Blewitt, C. W. Kreemer, and H.-P. Plag (2010), InSAR and GPS time series analysis: Crustal deformation in the Yucca Mountain, Nevada region, Abstract G13B-07 presented at 2010 Fall Meeting, AGU, San Francisco, Calif., 13–17 Dec.

Li, Z., J. R. Elliott, W. Feng, J. A. Jackson, B. E. Parsons, and R. J. Walters (2011), The 2010 MW 6.8 Yushu (Qinghai, China) earthquake: Constraints provided by InSAR and body wave seismology, *J. Geophys. Res.*, *116*, B10302, doi:10.1029/2011JB008358.

Lin, A., and M. Nishikawa (2007), Coseismic lateral offsets of surface rupture zone produced by the 2001 Mw 7.8 Kunlun earthquake, Tibet from the IKONOS and QuickBird imagery, *Int. J. Remote Sens.*, *28*(11), 2431–2445, doi:10.1080/01431160600647233.

Lin, A., et al. (2006), Average slip rate and recurrence internal of large magnitude earthquakes on western segment of the strike-slip Kunlun Fault, northern Tibet, *Bull. Seismol. Soc. Am.*, *96*(5), 1597–1611, doi:10.1785/0120050051.

Lorenzo-Martín, F., F. Roth, and R. Wang (2006), Inversion for rheological parameters from post-seismic surface deformation associated with the 1960 Valdivia earthquake, Chile, *Geophys. J. Int.*, *164*, 75–87, doi:10.1111/j.1365-246X.2005.02803.x.

Lundgren, P., et al. (2009), Southern San Andreas–San Jacinto fault system slip rates estimated from earthquake cycle models constrained by GPS and interferometric synthetic aperture radar observations, *J. Geophys. Res.*, *114*, B02403, doi:10.1029/2008JB005996.

Marone, C. J., C. H. Scholz, and R. Bilham (1991), On the mechanics of earthquake afterslip, *J. Geophys. Res.*, *96*, 8441–8452, doi:10.1029/91JB00275.

Massonnet, D., and K. L. Feigl (1998), Radar interferometry and its application to changes in the Earth's surface, *Rev. Geophys.*, *36*, 441–500, doi:10.1029/97RG03139.

Medvedev, S., and C. Beaumont (2001), Models for mid and lower crustal channel flows, *Eos Trans. AGU*, *82*(47), Fall Meet. Suppl., Abstract T12D-0937.

Mora, O., J. Mallorqui, and A. Broquetas (2003), Linear and nonlinear terrain deformation maps from a reduced set of interferometric SAR images, *IEEE Trans. Geosci. Remote Sens.*, *41*(10), 2243–2253, doi:10.1109/TGRS.2003.814657.

Okada, Y. (1985), Internal deformation due to shear and tensile faults in a half space, *Bull. Seismol. Soc. Am.*, *82*, 1018–1040.

Owens, T., and G. Zandt (1997), Implications of crustal property variations for models of Tibetan plateau evolution, *Nature*, *387*, 37–43, doi:10.1038/387037a0.

Parsons, B., et al. (2006), The 1994 Sefidabeh (eastern Iran) earthquakes revisited: New evidence from satellite radar interferometry and carbonate dating about the growth of an active fold above a blind thrust fault, *Geophys. J. Int.*, *164*, 202–217, doi:10.1111/j.1365-246X.2005.02655.x.

Peltzer, G., et al. (1998), Poroelastic rebound along the Landers 1992 earthquake surface rupture, *J. Geophys. Res.*, *103*, 30,131–30,145, doi:10.1029/98JB02302.

Peltzer, G., F. Crampe, and G. King (1999), Evidence of nonlinear elasticity of the crust from the Mw 7.6 Manyi (Tibet) earthquake, *Science*, *286*, 272–276, doi:10.1126/science.286.5438.272.

Pollitz, F. (1992), Postseismic relaxation theory on a spherical Earth, *Bull. Seismol. Soc. Am.*, *82*, 422–453.

Pollitz, F., G. Peltzer, and R. Bürgmann (2000), Mobility of continental mantle: Evidence from postseismic geodetic observations following the 1992 Landers earthquake, *J. Geophys. Res.*, *105*, 8035–8054, doi:10.1029/1999JB900380.

Pollitz, F., C. Wicks, and W. Thatcher (2001), Mantle flow beneath a continental strike-slip fault: Postseismic deformation after the 1999 Hector Mine earthquake, *Science*, *293*, 1814–1818, doi:10.1126/science.1061361.

Ren, J., and M. Wang (2005), GPS measured crustal deformation of the Ms 8.1 Kunlun earthquake on November 14th 2001 in Qinghai-Xizang plateau, *Quat. Sci.*, *25*, 34–44.

Rosen, P. A., et al. (2000), Synthetic aperture radar interferometry, *Proc. IEEE*, *88*, 333–382, doi:10.1109/5.838084.

Rosen, P. A., S. Hensley, and G. Peltzer (2004), Updated Repeated Orbit Interferometry package released, *Eos Trans. AGU*, *85*(5), 47, doi:10.1029/2004EO050004.

Royden, L. (1996), Coupling and decoupling of crust and mantle in convergent orogens: Implications for strain partitioning in the crust, *J. Geophys. Res.*, *101*, 17,679–17,705, doi:10.1029/96JB00951.

Ryder, I., et al. (2007), Post-seismic motion following the 1997 Manyi (Tibet) earthquake: InSAR observations and modeling, *Geophys. J. Int.*, *169*, 1009–1027, doi:10.1111/j.1365-246X.2006.03312.x.

Ryder, I., R. Bürgmann, and J. Sun (2010), Tandem afterslip on connected fault planes following the 2008 Nima-Gaize (Tibet) earthquake, *J. Geophys. Res.*, *115*, B03404, doi:10.1029/2009JB006423.

Ryder, I., R. Bürgmann, and F. Pollitz (2011), Low crustal relaxation beneath the Tibetan Plateau and Qaidam Basin following the 2001 Kokoxili earthquake, *Geophys. J. Int.*, *187*, 613–630, doi:10.1111/j.1365-246X.2011.05179.x.

Savage, J. C. (1990), Equivalent strike-slip earthquake cycles in half-space and lithosphere-asthenosphere Earth models, *J. Geophys. Res.*, *95*, 4873–4879, doi:10.1029/JB095iB04p04873.

Shen, Z.-K., et al. (2003), Postseismic deformation modeling of the 2001 Kokoxili earthquake, western China, paper presented at EGS-AGU-EUG Joint Assembly, Nice, France.

Stark, P. B., and R. L. Parker (1995), Bounded variable least squares: An algorithm and application, *Comput. Stat.*, *10*, 129–141.

Tapponnier, P., and P. Molnar (1977), Active faulting and tectonics in China, *J. Geophys. Res.*, *82*, 2905–2930, doi:10.1029/JB082i020p02905.

Toda, S., et al. (2005), Forecasting the evolution of seismicity in southern California: Animations built on earthquake stress transfer, *J. Geophys. Res.*, *110*, B05S16, doi:10.1029/2004JB003415.

van der Woerd, J., et al. (2002a), Uniform postglacial slip-rate along the central 600 km of the Kunlun Fault (Tibet), from Al^{26}, Be^{10}, and C^{14} dating of riser offsets, and climatic origin of the regional morphology, *Geophys. J. Int.*, *148*, 356–388, doi:10.1046/j.1365-246x.2002.01556.x.

van der Woerd, J., et al. (2002b), The 14 November 2001, Mw = 7.8 Kokoxili earthquake in northern Tibet (Qinghai province, China), *Seismol. Res. Lett.*, *73*(2), 125–135, doi:10.1785/gssrl.73.2.125.

Velasco, A., C. Ammon, and S. Beck (2000), Broadband source modeling of the November 8 1997, Tibet (Mw = 7.5) earthquake and its tectonic implications, *J. Geophys. Res.*, *105*, 28,065–28,080, doi:10.1029/2000JB900282.

Wang, H., M. Liu, J. Cao, X. Shen, and G. Zhang (2011), Slip rates and seismic moment deficits on major active faults in mainland China, *J. Geophys. Res.*, *116*, B02405, doi:10.1029/2010JB007821.

Wang, Q., et al. (2001), Present-day crustal deformation in China constrained by Global Positioning System measurements, *Science*, *294*, 574–577, doi:10.1126/science.1063647.

Wang, R., F. Lorenzo-Martín, and F. Roth (2006), PSGRN/PSCMP—A new code for calculating co- and post-seismic deformation, geoid and gravity changes based on the viscoelastic-gravitational dislocation theory, *Comput. Geosci.*, *32*, 527–541, doi:10.1016/j.cageo.2005.08.006.

Wen, X., G. Yi, and X. Xu (2007), Background and precursory seismicities along and surrounding the Kunlun fault before the Ms 8.1, 2001, Kokoxili earthquake, China, *J. Asian Earth Sci.*, *30*, 63–72, doi:10.1016/j.jseaes.2006.07.008.

Wessel, P., and W. H. F. Smith (1998), New, improved version of Generic Mapping Tools released, *Eos Trans. AGU*, *79*(47), 579, doi:10.1029/98EO00426.

Williams, S., Y. Bock, and P. Fang (1998), Integrated satellite interferometry: Tropospheric noise, GPS estimates and implications for interferometric synthetic aperture radar product, *J. Geophys. Res.*, *103*(B11), 27,051–27,067, doi:10.1029/98JB02794.

Wright, T. J., Z. Lu, and C. Wicks (2003), Source model for the Mw 6.7, 23 October 2002, Nenana Mountain earthquake (Alaska) from InSAR, *Geophys. Res. Lett.*, *30*(18), 1974, doi:10.1029/2003GL018014.

Xu, X., et al. (2006), Reevaluation of surface parameters and faulting segmentation of the 2001 Kunlunshan earthquake (Mw 7.8), northern Tibetan Plateau, *J. Geophys. Res.*, *111*, B05316, doi:10.1029/2004JB003488.

Yeats, R. S., K. Sieh, and C. R. Allen (1997), *The Geology of Earthquakes*, Oxford Univ. Press, New York.

Yin, A., and T. Harrison (2000), Geologic evolution of the Himalayan-Tibetan orogen, *Annu. Rev. Earth Planet. Sci.*, *28*, 211–280, doi:10.1146/annurev.earth.28.1.211.

Zhang, C., J. Cao, and Y. Shi (2009), Studying the viscosity of lower crust of Qinghai-Tibet Plateau according to post-seismic deformation, *Sci. China, Ser. D*, *52*(3), 411–419, doi:10.1007/s11430-009-0028-9.

Zhang, P.-Z., et al. (2004), Continuous deformation of the Tibet Plateau from global positioning system data, *Geology*, *32*(9), 809–812, doi:10.1130/G20554.1.

Zhu, L., and D. V. Helmberger (1998), Moho offset across the northern margin of the Tibetan Plateau, *Science*, *281*, 1170–1172, doi:10.1126/science.281.5380.1170.